

Herschel/HIFI observations of [C II] and [¹³C II] in PDRs^{*}

V. Ossenkopf¹, M. Röllig¹, D.A. Neufeld², P. Pilleri^{3,4}, D.C. Lis⁵, A. Fuente³, F.F.S. van der Tak^{6,7}, E. Bergin⁸

¹ I. Physikalisches Institut, Universität zu Köln, Zùlpicher Str. 77, D-50937 Köln, Germany
e-mail: ossk@ph1.uni-koeln.de

² Department of Physics and Astronomy, Johns Hopkins University, 3400 North Charles Street, Baltimore, MD 21218, USA

³ Observatorio Astronómico Nacional, Apdo. 112, E-28803 Alcalá de Henares (Madrid), Spain

⁴ Centro de Astrobiología (INTA-CSIC), Ctra. M-108, km. 4, E-28850 Torrejón de Ardoz, Spain

⁵ California Institute of Technology, Cahill Center for Astronomy and Astrophysics 301-17, Pasadena, CA 91125 USA

⁶ SRON Netherlands Institute for Space Research, Landleven 12, 9747 AD Groningen, The Netherlands

⁷ Kapteyn Astronomical Institute, University of Groningen, PO box 800, 9700 AV Groningen, The Netherlands

⁸ University of Michigan, Ann Arbor, MI 48197 USA

Preprint online version: August 8, 2018

ABSTRACT

Context. Chemical fractionation in the interstellar medium can create isotopologue abundance ratios that differ by many orders of magnitude from the normal isotopic abundance ratios. By understanding how these differences are reflected in astronomical observations under various conditions, we try to obtain a new tool to sensitively probe these conditions.

Aims. Recently, we introduced detailed isotopic chemistry into the KOSMA- τ model for photon-dominated regions (PDRs) to give theoretical predictions for the abundance of the carbon isotopologues as a function of PDR parameters. Combined with radiative transfer computations for specific geometries, we estimated the possible intensity ratio of the [C II]/[¹³C II] lines. Here, we compare these predictions with new Herschel observations.

Methods. We performed Herschel/HIFI observations of the [C II] 158 μ m line in a number of PDRs. In all sources we observed at least two hyperfine components of the [¹³C II] transition allowing to determine the [C II]/[¹³C II] intensity ratio, after some revision of the intrinsic hyperfine ratios. Comparing the intensity ratios with the results from the updated KOSMA- τ model, we identify cases dominated by chemical fractionation and cases dominated by the optical depth of the main isotopic line.

Results. An observable enhancement of the [C II]/[¹³C II] intensity ratio due to chemical fractionation depends mostly on geometry and velocity structure, and less on the gas density and radiation field. It is expected to be at maximum for PDR layers that are somewhat shielded from UV radiation, but not hidden by surface layers of optically thick [C II]. In our observations the [C II]/[¹³C II] ratio for the integrated line intensity was always dominated by the optical depth of the main isotopic line. However, an enhanced intensity ratio is found for particular velocity components in a few sources: the red-shifted material in the ultracompact H II region Mon R2, the wings of the turbulent profile in the Orion Bar, and possibly a blue wing in NGC 7023. The mapping of the [¹³C II] lines in the Orion Bar allows to derive a C⁺ column density map confirming the temperature stratification of the C⁺ layer, in agreement with the chemical stratification of the Bar.

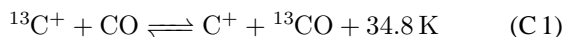
Conclusions. Carbon fractionation can be significant, even in relatively warm PDRs, but a resulting enhanced [C II]/[¹³C II] intensity ratio is only observable for special configurations. In most cases, a reduced [C II]/[¹³C II] intensity ratio can be used instead to derive the [C II] optical depth to achieve reliable column density estimates that can be compared with PDR models. The C⁺ column densities for all sources show that at the position of the [C II] peak emission, a dominant fraction of the gas-phase carbon is in the form of C⁺.

Key words. ISM: abundances – ISM: structure – ISM: clouds

1. Introduction

The isotopic abundance ratios of elements such as C, N and O in the interstellar medium reflect the star formation history of the environment, and observations of molecular isotopic line ratios at (sub)mm wavelengths are a common way to measure this effect (e.g. Wilson 1999).

Isotopic fractionation of carbon in the interstellar medium, i.e. the ¹²C/¹³C ratio in various species, is driven mainly through the fractionation reaction



providing a significant energy excess for binding the ¹³C to the oxygen (Langer et al. 1984). Thus chemical fractionation

* Herschel is an ESA space observatory with science instruments provided by European-led Principal Investigator consortia and with important participation from NASA.

of carbon is important even for relatively warm gas, as long as there is a significant fraction of ionized carbon available¹. The reaction (C 1) favors formation of ¹³CO and depletion of ¹³C⁺ at low temperatures, shifting the fractional abundances of the two species relative to the normal solar isotopic ratio, but competes with isotope-selective dissociation governed by a different shielding through dust, H₂ and other CO isotopologues (Visser et al. 2009).

A systematic discussion of the observational results on carbon fractionation was provided by Keene et al. (1998) for dense molecular clouds and Liszt (2007) with emphasis on more diffuse clouds. Through observations of [¹³C I] and ¹³C¹⁸O in the Orion Bar Keene et al. (1998) found little evidence for chemical fractionation, but noticed a contradiction between the chem-

¹ All other fractionation reactions for ¹³C have lower excess energies, therefore being relevant only in cold gas.

ical models predicting a slight relative enhancement of ¹³C, but a reduction of ¹³C¹⁸O while the observations showed the opposite behavior. In contrast to the CO results, Sakai et al. (2010) found clear evidence for fractionation in C₂H under the dark cloud conditions of TMC 1. In line with previous results (Sonnentrucker et al. 2007; Sheffer et al. 2007; Burgh et al. 2007) Liszt (2007) summarized the clear indications for fractionation of CO in translucent and diffuse clouds. They confirmed that the fractionation reaction (C 1) dominates the carbon chemistry for densities $n_{\text{H}_2} \geq 100 \text{ cm}^{-3}$ and provided new reaction rates for low temperatures, but also showed the importance of the CO destruction in reactions with He⁺ for lower densities.

In paper I (Röllig & Ossenkopf 2012), we present results from the update of the KOSMA- τ model for photon-dominated regions (PDRs) to the full isotopic chemistry, providing isotopologue ratios for various species. Comparing the fractionation ratio of the ¹²C⁺/¹³C⁺ abundances with the elemental isotopic ratio, we note that

- the fractionation ratio is always higher than or equal to the elemental ratio, i.e. ¹³C⁺ is always underabundant with respect to C⁺.
- the fractionation ratio equals the elemental ratio at low A_V , but increases significantly towards larger A_V .

These are direct consequences of reaction (C 1). No other important reaction or isotope-selective photodestruction acts in the opposite direction. At low A_V , temperatures are usually high enough so that the excess energy plays no role, but once the temperature drops below 50 K the back reaction becomes less probable and the fractionation ratio increases rapidly. It stays at high values as long as enough ¹³C⁺ ions are available to feed the reaction. Deep into the cloud interiors, these ions are formed through the dissociative reaction He⁺ + ¹³CO. The fractionation ratio is then controlled by cosmic ray ionization providing a roughly constant ¹²C⁺/¹³C⁺ enhancement.

However, two competing processes change the [C II]/[¹³C II] ratio in PDRs: chemical fractionation raises the [C II]/[¹³C II] intensity ratio relative to the elemental abundance ratio, while the optical depth of the main isotopic line lowers its intensity relative to the [¹³C II] transitions.

[¹³C II] was first resolved by early heterodyne observations at the Kuiper Airborne Observatory (KAO, e.g. Boreiko et al. 1988; Boreiko & Betz 1996) showing no increase of the corresponding [C II]/[¹³C II] intensity ratio, but a reduction relative to the isotopic elemental ratio corresponding to a significant optical depth of the main isotopic line reducing the intensity ratio. With the low spatial and velocity resolution of these observations, it was, however, impossible to determine whether this average reduction represents all density or velocity components in the beam or whether individual components are dominated by either of the two competing processes. Only from additional observations with high velocity resolution preferentially covering varying conditions it is therefore possible to separate the impact of the two processes in PDRs.

The HIFI instrument (de Graauw et al. 2010) on-board the Herschel satellite (Pilbratt et al. 2010) allowed for the first time to systematically observe [¹³C II] with a good sensitivity and high spatial resolution in a number of objects. This allows to study the ¹²C/¹³C ratio in different environments by comparing the observations with the theoretical predictions. We detected [¹³C II] in four bright PDRs, allowing to look for the signature of chemical carbon fractionation in the warm PDR gas or to determine the optical depth and column density of C⁺.

In Sect. 2 we elaborate on the detailed theoretical predictions for ¹²C⁺/¹³C⁺ and the resulting intensity ratio [C II]/[¹³C II] under varying physical conditions in the frame of the KOSMA- τ PDR model. In Sect. 3 we present the HIFI observations of [C II] and [¹³C II]. Section 4 discusses the observational results for the Orion Bar, Mon R2, NGC 3603, Carina, and NGC 7023 and Sect. 5 concludes with a summary of the matches and discrepancies.

2. Model predictions for the [C II]/[¹³C II] ratio

The development of theoretical models for PDRs is an active field of research because of the complex interplay of geometrical constraints, properties of the UV field, and chemical and physical processes in the gas (Röllig et al. 2007). Because of this complexity, all models with an elaborated description of the PDR chemistry are currently restricted to one-dimensional geometries, therefore describing PDRs either as plane-parallel slabs or as (ensemble of) spheres. However, real sources like the prototypical PDR of the Orion Bar, show more complex geometries, containing elements of both descriptions, e.g. a large-scale plane-parallel configuration superimposed on a clumpy small-scale structure, better described by an ensemble of spherical cores (see e.g. Hogerheijde et al. 1995).

We consider both limiting cases in the frame of the KOSMA- τ PDR model, a code designed to simulate spherical clumps, where we can approximate a plane-parallel PDR by considering very massive clumps ($M \geq 100 M_{\odot}$) that form an almost plane-parallel structure in their outer layers. This approach allows us to use the new implementation of the fractionation network in the KOSMA- τ PDR model code and to easily compare the results with other PDR models (see Röllig et al. 2007) that lack isotope networks so far.

2.1. Model setup

The KOSMA- τ PDR model assumes a spherical cloud geometry exposed to isotropic UV illumination, measured in units of the interstellar radiation field, χ_0 (Draine 1978). Model parameters are the hydrogen density at the surface, n_{surf} , UV field, χ , and cloud mass, M . The density structure assumes a power law increase, $n_H(r) = n_{\text{surf}}(r/R_0)^{-1.5}$, from the surface to 1/5 of the outer radius, R_0 , and a constant density further in. For the results presented here, we keep the metallicity at solar values and assume a standard elemental isotopic ratio of ¹²C/¹³C of 67 (Wakelam & Herbst 2008). The actual elemental isotopic ratio is subject to systematic variations with galactocentric radius (Wilson 1999) but all the sources discussed in Sect. 3.2 have approximately solar galactocentric radii. However, even within the solar neighborhood there exist noticeable variations with values between 57 and 78 where the value of 67 matches the ratio observed in Orion (Langer & Penzias 1990, 1993). We therefore assume an error bar of up to 15% for the elemental abundance ratio.

The PDR model iteratively computes the steady-state chemistry, the local cooling and heating processes, and the radiative transfer to predict the density of the different species and the intensity of the line and continuum radiation emitted by them.

The restriction of the code to an isotropic illumination is not a fundamental limitation when comparing different geometries. The penetration of an isotropic radiation field can be computed from the penetration of a uni-directional radiation field by rescaling the optical depth according to the formalism

from Flannery et al. (1980) and vice versa. Röllig et al. (2007) showed a very good match of the different PDR models when the rescaling was applied. When re-interpreting the KOSMA- τ results for a uni-directional illumination, one thus has to stretch the width of the outer layers relative to the given scale.

2.2. The effect of chemical fractionation on the [C II]/ $^{13}\text{C II}$ ratio

Paper I already provides some predictions for clump-integrated intensities for ^{13}C -bearing species for the special configuration of a spherical PDRs. To understand in detail how the chemical fractionation structure can translate into an observable [C II]/ $^{13}\text{C II}$ intensity ratio, we investigate here how the depth-dependent carbon fractionation translates into a varying local $^{13}\text{C II}$ and [C II] emissivity, using the simplified picture of a plane-parallel configuration described by two parameters only: the density and the impinging UV field. In the resulting one-dimensional PDR, different layers reflect a decreasing UV penetration. This allows us to disentangle the relative contributions of these layers to the observable [C II]/ $^{13}\text{C II}$ intensity ratio. The approach ignores all effects resulting from the uncertain details of the cloud geometries and of the optical depth of the line along the line of sight to the observer in a particular geometry.

Fig. 1 shows the temperature and abundance structure of the dominating carbon bearing species and the resulting [C II] and $^{13}\text{C II}$ line emissivity as a function of the relative radius – or depth from the surface into the cloud, respectively – for an example model with a density at cloud surface of 10^4 cm^{-3} and a radiation field of $1000\chi_0$. The local [C II] line emissivity can be computed in terms of a two-level system

$$\int \epsilon dv = \frac{hc^3 A}{8\pi k\nu^2} \times N_{\text{C}^+} \frac{g_u \exp(-\Delta E/kT_{\text{ex}})}{g_l + g_u \exp(-\Delta E/kT_{\text{ex}})} \quad (1)$$

with $\Delta E = h\nu = k \times 91.2\text{K}$, the statistical weights $g_u = 4$ and $g_l = 2$, and the Einstein- A coefficient of $A = 2.3 \times 10^{-6} \text{ s}^{-1}$ (Wiese & Fuhr 2007), providing

$$\int \epsilon dv \approx 1011 \frac{\text{K km s}^{-1}}{\text{cm}^{-3} \text{ pc}} \times N_{\text{C}^+} \frac{2 \exp(-91.2\text{K}/T_{\text{ex}})}{1 + 2 \exp(-91.2\text{K}/T_{\text{ex}})} \quad (2)$$

and we obtain the excitation temperature T_{ex} from the detailed balance including collisional excitation through H_2 (Flower & Launay 1977), atomic hydrogen (Launay & Roueff 1977), and electrons (Wilson & Bell 2002) and radiative de-excitation and trapping². For $^{13}\text{C II}$, this approach sums over all hyperfine components. The emissivity represents the integrated line intensity per hydrogen column density without optical depth correction.

In this example model, most of the [C II] emission stems from the cloud surface where all carbon is in ionized form and at high temperatures the $\text{C}^+/\text{}^{13}\text{C}^+$ fractionation ratio is equal to the elemental isotopic abundance ratio so that the [C II]/ $^{13}\text{C II}$ intensity ratio also matches the elemental ratio. Deep inside the cloud, where most of carbon is in the form of CO and $^{13}\text{C}^+$ is only produced by cosmic ray ionized He^+ , the intensity ratio is enhanced by about a factor of ten relative to the elemental isotopic ratio, but the C^+ abundance is reduced by six orders of magnitude so that the enhanced ratio is hidden by the surface emission. The region where chemical fractionation may be detectable is the transition zone from C^+ to CO where the

² $1011 \text{ K km s}^{-1} = 7.11 \times 10^{-3} \text{ ergs}^{-1} \text{ cm}^{-2} \text{ sr}$ at the frequency of the [C II] transition

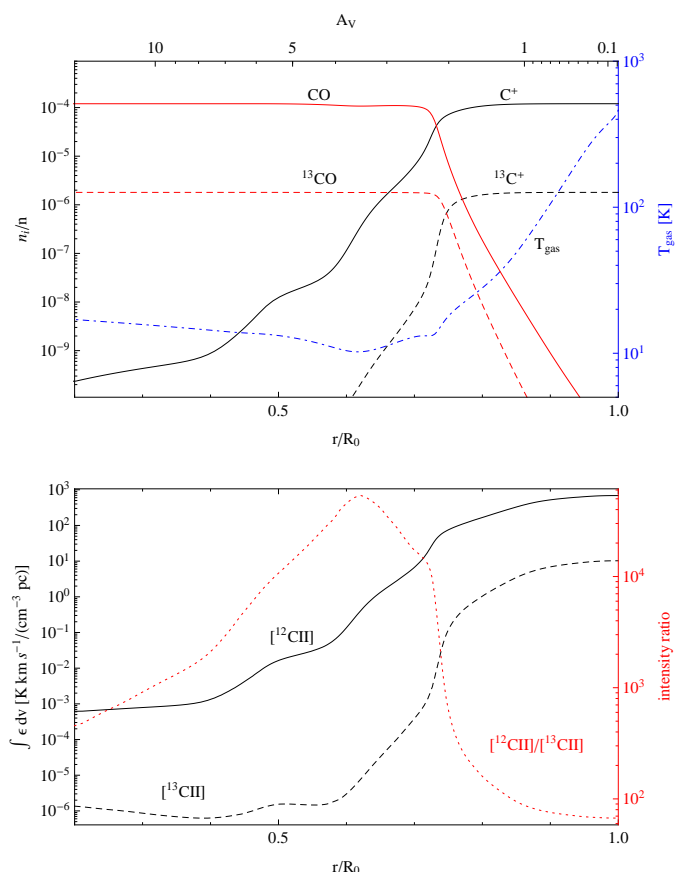


Fig. 1. Top: Abundance distribution of C^+ and CO and the corresponding ^{13}C isotopologues for a model with $n_{\text{surf}} = 10^4 \text{ cm}^{-3}$, $1000 \chi_0$ and $1000 M_{\odot}$. The blue curve shows the corresponding gas temperature structure determining the emissivity. **Bottom:** Resulting integrated optically thin line emissivity $\int \epsilon dv$ in $\text{K km s}^{-1}/(\text{cm}^{-3} \text{ pc})$ for the [C II] and $^{13}\text{C II}$ lines (black curves) as a function of the clump radius. The red line shows the intensity ratio provided by the two curves.

$\text{C}^+/\text{}^{13}\text{C}^+$ fractionation ratio amounts to a few hundred and the intensity is only a factor ten weaker than at the surface (around $r/R_0 = 0.73$ in Fig. 1). The actual emissivity ratio can be boosted to values above the fractionation ratio by radiative excitation of C^+ in the cool and darker inner regions. As C^+ “feels” the strong line emission from the clump surface, it gains excitation temperatures above the kinetic temperature while the $^{13}\text{C II}$ excitation temperature closely follows the kinetic temperature. Due to the exponential term in Eq. 2 this can provide up to a factor ten enhancement of the [C II]/ $^{13}\text{C II}$ intensity ratio for cold gas at moderate densities deeper in the cloud.

To better evaluate for which conditions we might observationally detect chemical fractionation, we compute the difference between the [C II] emissivity and the $^{13}\text{C II}$ emissivity scaled by the elemental abundance ratio. This quantity does not directly reflect the intensity ratio, as shown in Fig. 1, but enhancements in this difference indicate conditions under which an increased $\text{C}^+/\text{}^{13}\text{C}^+$ fractionation ratio eventually turns into an observable increased [C II]/ $^{13}\text{C II}$ intensity ratio. Figure 2 shows the emissivity difference as a function of the distance from the outer radius for varying PDR parameters. In the upper panel, we vary the gas density for a constant radiation field of $1000\chi_0$ while the lower panel shows the impact of dif-

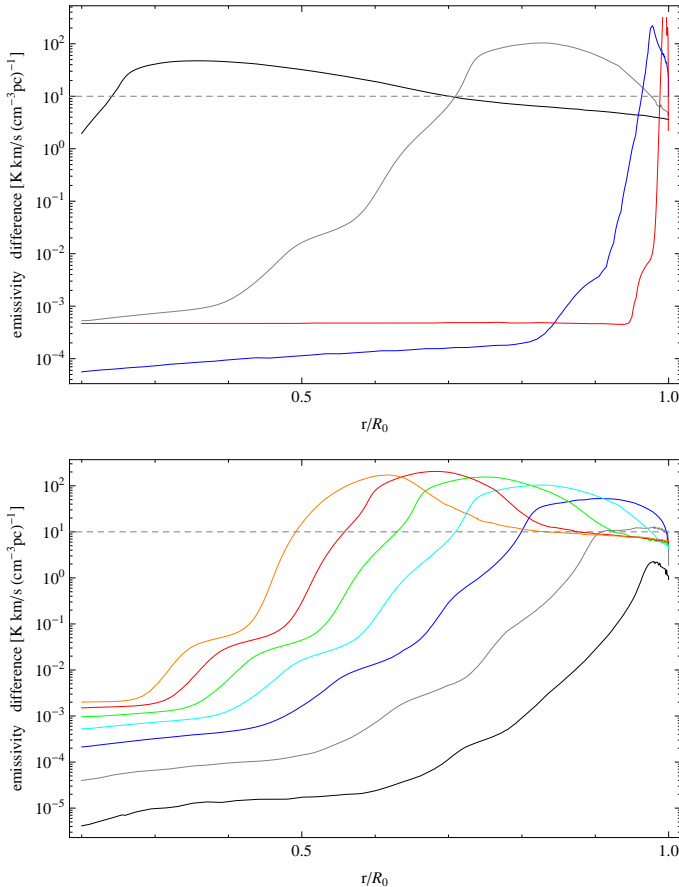


Fig. 2. Differences between [C II] emissivity and [¹³C II] emissivity multiplied by the standard elemental isotopic ratio of 67 showing conditions where a increased C⁺/¹³C⁺ fractionation ratio turns into an observable increased [C II]/[¹³C II] intensity ratio. The upper plot uses a radiation field of 1000χ₀ and varies the surface gas density: 10³ cm⁻³ (black), 10⁴ cm⁻³ (grey), 10⁵ cm⁻³ (blue), 10⁶ cm⁻³ (red). The lower plot uses a gas density of $n_{\text{surf}} = 10^4$ cm⁻³ and varies the radiation field: 1χ₀ (black), 10χ₀ (grey), 100χ₀ (blue), 10³χ₀ (cyan), 10⁴χ₀ (green), 10⁵χ₀ (red), 10⁶χ₀ (orange). The dashed line at 10 K km s⁻¹ (cm⁻³ pc)⁻¹ gives a rough indication what differences might be observable with current technology in a deep integration.

ferent radiation fields for a constant gas density of $n_{\text{surf}} = 10^4$ cm⁻³. Whenever the difference is lower than about 1 K km s⁻¹ (cm⁻³ pc)⁻¹ no [C II] enhancement is practically observable, either because the [¹³C II] emission is too weak or because there is no enhanced C⁺/¹³C⁺ fractionation ratio. Three factors determine the detectability of an enhanced fractionation ratio in the optically thin picture. The radiation field has to be strong enough to produce a significant column of ionized carbon, the corresponding layer has to be cool enough so that the reaction (C 1) is effective, and the layer of enhanced C⁺/¹³C⁺ needs to be thick enough to provide a significant beam filling in a finite telescope beam. Paper I has shown that these conditions can be met for a wide variety of conditions, provided that there is a sufficient mass of dense gas. With at least 1 M_{\odot} at densities of 10⁴ cm⁻³ a significant fractionation layer occurs even at high UV fields. In the upper panel of Figure 2 we see, however, that at densities of 10⁵ cm⁻³ or above, the C⁺-CO transition region, producing an enhanced [C II]/[¹³C II] intensity ratio associated

with strong emission, is very thin. The lower panel shows that we find only small [C II] intensities from clumps exposed to radiation fields of 10χ₀ or below, making every [C II] observation difficult. At all higher radiation fields, fractionation should be detectable. When considering the full parameter range, we find some degeneracy in the sense that for higher densities fractionation may also be observable at low UV fields. The ideal environment for an increased C⁺/¹³C⁺ fractionation ratio is thus the mildly shielded gas in classical PDRs with $\chi \gtrsim 100\chi_0$ and densities in the order of 10⁴ – 10⁵ cm⁻³.

2.3. Radiative transfer effects on the [C II]/[¹³C II] ratio

The [C II] optical depth can be computed in the same way as the emissivity (Eq. 2) through

$$\int \tau dv = 7.15 \times 10^{-18} \frac{\text{kms}^{-1}}{\text{cm}^{-2}} \times N_{\text{C}^+} \frac{1 - \exp(-91.2\text{K}/T_{\text{ex}})}{1 + 2 \exp(-91.2\text{K}/T_{\text{ex}})} \approx 7.15 \times 10^{-18} \frac{\text{kms}^{-1}}{\text{cm}^{-2}} \times N_{\text{C}^+} \frac{32.9\text{K}}{T_{\text{ex}}}. \quad (3)$$

For a Gaussian velocity distribution this is equal to

$$\int \tau dv = \frac{1}{2} \sqrt{\frac{\pi}{\ln 2}} \Delta v \times \hat{\tau} \quad (4)$$

where $\hat{\tau}$ denotes the peak optical depth and Δv the FWHM of the velocity distribution.

Vice versa, we can determine the optical depth from a measured [C II]/[¹³C II] intensity ratio (IR), at any given frequency in the line when knowing the C⁺/¹³C⁺ fractionation ratio (FR), assuming optically thin [¹³C II] lines, and assuming equal excitation temperatures of [C II] and [¹³C II]:

$$\frac{IR_{\nu}}{FR} = \frac{1 - \exp(-\tau_{[\text{C II}]})}{\tau_{[\text{C II}]}} \quad (5)$$

For the line integrated intensity ratio, one has to take the broadening of the [C II] line due to the optical depth into account. For a Gaussian velocity distribution and a line-center optical depth $\hat{\tau} < 10$, the increase of the line width can be linearly approximated by the simple factor $1 + 0.115\hat{\tau}$, and the average optical depth measured through the integrated line intensity is³

$$\langle \tau \rangle \approx 0.64\hat{\tau}. \quad (6)$$

To quantify the impact of the line-of-sight optical depth on the [C II]/[¹³C II] intensity ratio we have to switch from the semi-infinite plane-parallel description to a finite geometry, containing a description for the C⁺ column density, not only in the direction towards the illuminating source, but also in the line of sight towards the observer. This is naturally taken into account when using the clumpy picture that forms the base of the KOSMA- τ model, i.e. considering the case of spherical PDRs. It introduces the clump mass, i.e. the absolute radius of the clump, as a third independent parameter⁴. By integrating over the full volume of each clump and averaging the intensity over the projected area of the spherical model clumps, we mimic the situation of a fractal cloud, consisting of an ensemble of

³ The general, more complex expression, also covering the large optical depth limit, is given e.g. by Phillips et al. (1979).

⁴ We do not include a separate interclump medium, but rather represent interclump material by the equivalent mass of an ensemble of small, transient, low-density clumps.

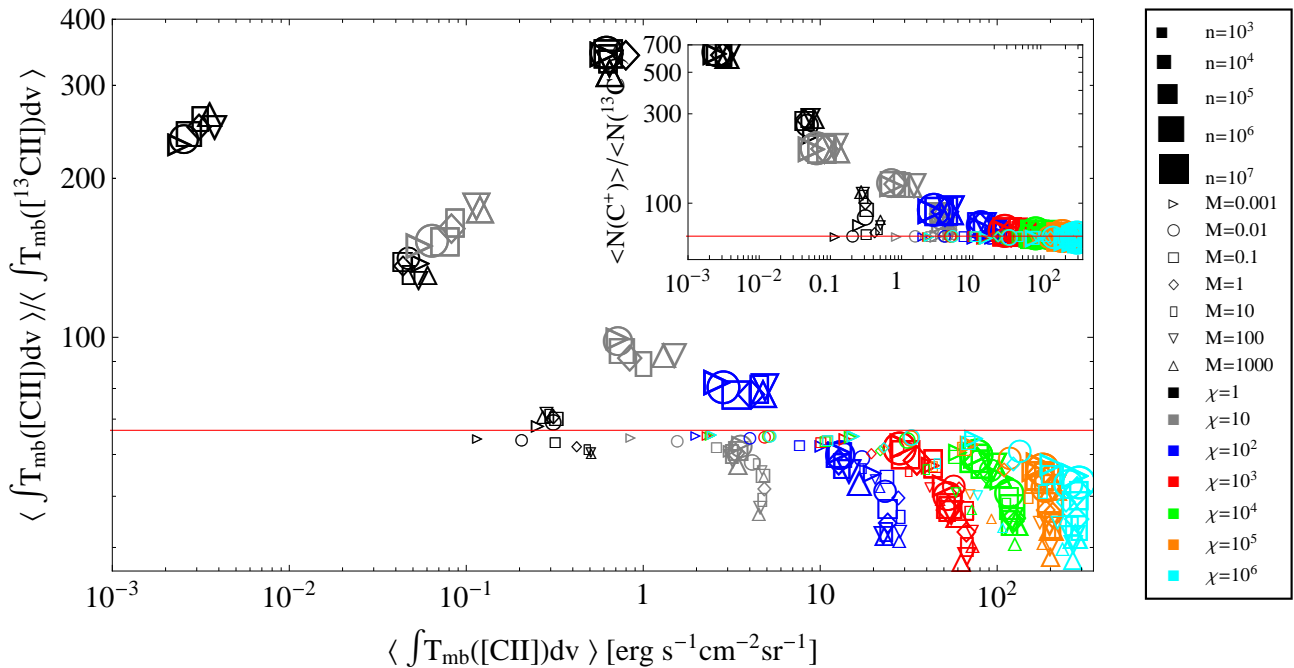


Fig. 3. Clump integrated intensity ratio $\int I([\text{C II}])dv / \int I(^{13}\text{C II})dv$ vs. [C II] intensity from the KOSMA- τ model for different parameters. The model parameters n , M , and χ , are coded as size, shape, and color of the respective symbols. The red horizontal line denotes the assumed elemental abundance ratio $^{12}\text{C}/^{13}\text{C}$ of 67. The insert demonstrates the underlying column density ratio for the different clumps. For $^{13}\text{C II}$, we sum over all hyperfine components.

many clumps, where individual structures cannot be resolved (Stutzki et al. 1998).

In Fig. 3 we compare the ratio of clump averaged integrated line intensities, $\int I([\text{C II}])dv / \int I(^{13}\text{C II})dv$ for a wide range of densities, clump masses and impinging radiation fields. The insert shows the underlying mean column density ratio for the clumps producing the observed intensity ratio (see paper I).

While the column density ratio falls above the elemental isotopic ratio for all model clumps, this does not hold for the $[\text{C II}]/^{13}\text{C II}$ intensity ratio. Models with low densities and all models with $\chi > 100$ show an intensity ratio below the elemental ratio, down to a value of 38. In these models, the fractionation ratio in the column densities is close to the elemental ratio so that the reduced intensity ratio is a direct measure of the average optical depth of the main isotopic line through Eq. 5. The reduction of the line integrated intensity ratio by a factor two corresponds to a moderate [C II] optical depth, $\langle \tau \rangle \approx 1.6$ or $\hat{\tau} \approx 2.5$, respectively, for the individual clumps. That means that in all models exposed to high UV fields an ionized carbon layer of about the same column density is formed, independent of the other clump parameters. This is naturally explained by the transition from C^+ to CO at about $A_V \approx 0.2$. Different PDR parameters only change the physical depth and temperature of this transition point. Higher [C II] optical depths only occur if multiple clumps add up their optical depth on the line of sight at the same velocity without mutual shielding of the impinging UV field, i.e. in special geometries.

In the clump-integrated picture, only models with low UV field χ and high densities trace the chemical fractionation, showing an intensity ratio that is enhanced relative to the elemental abundance ratio. A detailed comparison shows that even for those clumps some line saturation occurs, so that the intensity ratio does not measure the true $\text{C}^+ / ^{13}\text{C}^+$ fractionation ratio,

but falls somewhat below it. This result is in contrast to the pure emissivity considerations in Sect. 2.2 that indicated that medium-density clumps produce an enhanced intensity ratio.

Optical depth effects are always significant in the considered geometry with similar column densities of C^+ towards the illuminating sources and towards the observer. C^+ is abundant down to a shielding gas and dust column of $A_V \approx 1$ (see Fig. 1). If all carbon is ionized in this column, it provides $N_{\text{C}^+} \approx 2.5 \times 10^{17} \text{ cm}^{-2}$, corresponding to a [C II] optical depth of 0.8 for a slightly subthermal excitation temperature of $T_{\text{ex}} = 50 \text{ K}$ and the line width of 1.5 km s^{-1} used in the model. That means that in isotropic configurations with narrow lines, as in the clumpy PDR model, [C II] always turns slightly optically thick when the condition for an efficient fractionation is met. Hence, we find a relatively constant [C II] optical depth of 0.8–1.6 for all clumps that are big enough to contain the critical column for $A_V = 1$ and that are exposed to a radiation field strong enough to ionize the carbon. As a consequence, we expect a behavior as in Fig. 3 for isotropic PDRs with narrow velocity distributions. Most of the fractionation effect in the $\text{C}^+ / ^{13}\text{C}^+$ abundance ratio that was seen in the local $[\text{C II}]/^{13}\text{C II}$ emissivity ratio in Sect. 2.2, is therefore hidden from the observer by an optical depth close to unity in this case.

A recovery of the true fractionation ratio, i.e. the $\text{C}^+ / ^{13}\text{C}^+$ column densities, through the observable $[\text{C II}]/^{13}\text{C II}$ intensity ratio requires optically thin [C II] emission, either through a much wider velocity dispersion, reducing the [C II] optical depth in a broader line (see Eq. 4), or an anisotropic geometry that provides a higher column of gas for the UV shielding than in the line-of-sight towards the observer. Only in these configurations we can expect to detect chemical fractionation through the $[\text{C II}]/^{13}\text{C II}$ ratio matching the predictions from Sect. 2.2. In contrast we may also find edge-on configurations with a larger

column on the line of sight towards the observer than towards the illuminating sources (see the Orion Bar in Sect. 4.1) where the [C II] optical depth may grow beyond 2 providing an intensity ratio much below the local C⁺/¹³C⁺ fractionation ratio.

Altogether, we must conclude that in most typical PDRs with bright [C II] emission, no significant fractionation is expected to appear in the C⁺ column densities, i.e. the fractionation ratio will match the elemental abundance ratio while the intensity ratio is dominated by the optical depth of the [C II] line pushing it below the elemental ratio. In those cases we can only use the intensity ratio to compute the C⁺ column density through Eqs. (5) and (3). This is an essential parameter to compare with models for deriving e.g. the ionization degree or the photoelectric heating efficiency. Some carbon fractionation may be detectable through an increased [C II]/[¹³C II] intensity ratio compared to the elemental abundance ratio for sources with high densities and moderate UV fields in case of a favorable geometry or relatively broad velocity distributions. However, even in these cases it may be impossible to deduce the exact C⁺/¹³C⁺ fractionation ratio due to the superimposed optical depth effects.

3. Observations

3.1. [¹³C II] spectroscopy

C⁺ has a single fine structure transition, [C II] ²P_{3/2} – ²P_{1/2}, at 1900.537 GHz, which for ¹³C⁺ is split into three hyperfine components due to the unbalanced additional neutron spin. The frequencies of these transitions have been determined by Cooksy et al. (1986) based on the combination of laser magnetic resonance measurements with ab-initio computations of Schaefer & Klemm (1970). Our observations from Sect. 4.1.2 confirm these frequencies with an accuracy of about 3 MHz, as the relatively narrow [C II] and [¹³C II] lines in the Orion Bar match each other and numerous other molecular transitions to within 0.5 km s⁻¹ in velocity space when using these rest frequencies.

We have computed the relative line strengths expected for the three hyperfine transitions in local thermodynamic equilibrium (LTE), which – for a magnetic dipole transition – are given by

$$S_{\text{hfs}} = \frac{(2F' + 1)(2F + 1)}{2I + 1} \left\{ \begin{matrix} J & F & I \\ F' & J' & 1 \end{matrix} \right\}^2 \quad (7)$$

(Eq. 8 in Garstang (1995), normalized to unity). Here, $J' = 3/2$ and $J = 1/2$ are the total electronic angular momenta for the upper and lower states, $I = 1/2$ is the nuclear spin of the ¹³C nucleus, F' and F are the total angular momenta (including nuclear spin) for the upper and lower states, and the curly brackets denote a Wigner 6j-symbol. This expression – which rests on the standard assumptions that magnetic dipole (M1) radiation dominates over electric quadrupole (E2) radiation, and that the Hamiltonian commutes with all relevant angular momentum operators – yields a ratio of 0.625 : 0.25 : 0.125 for the $F' - F = 2 - 1 : 1 - 0 : 1 - 1$ transitions⁵. All spectroscopic parameters are summarized in Table 1.

⁵ Our line ratios differ from those (0.444 : 0.356 : 0.20) given by Cooksy et al. (1986) and used in previous astronomical studies. This discrepancy may account for the anomaly reported recently by Graf et al. (2012), who observed a $F = 2 - 1 : F = 1 - 0$ ratio in NGC 2024 that was considerably larger than that predicted by Cooksy et al. (1986). It also requires a minor revision to the elemental isotopic ratio inferred by Boreiko & Betz (1996) from observations of the $F = 2 - 1$ and $1 - 0$ transitions observed toward M42. That study ap-

Table 1. Spectroscopic parameters of the [¹³C II] ²P_{3/2} – ²P_{1/2} transition

line	ν [GHz]	g_u	g_l	relative intensity
$F = 2 - 1$	1900.466	5	3	0.625
$F = 1 - 0$	1900.950	3	1	0.250
$F = 1 - 1$	1900.136	3	3	0.125

3.2. HIFI measurements

We performed [¹³C II] observations with the HIFI instrument (de Graauw et al. 2010) on-board the Herschel satellite (Pilbratt et al. 2010) towards four bright PDRs in the framework of the key projects HEXOS (Bergin & Herschel Hexos Team 2011) and WADI (Ossenkopf et al. 2011). The first region is the Orion Bar (map center: 5^h35^m20.81^s, –5°25'17.1"), an edge-on, almost linear PDR at a distance of 415 pc (Menten et al. 2007), formed by material of the Orion Molecular Cloud 1 (OMC-1) exposed to the radiation from the Trapezium cluster providing an FUV flux of 4 – 5 × 10⁴χ₀ in terms of the Draine (1978) field. Previous, spectrally unresolved observations of [C II] in the Orion Bar have been carried out by Stacey et al. (1993) and Herrmann et al. (1997) using the Kuiper Airborne Observatory (KAO). In terms of a pure edge-on configuration, the Orion Bar PDR is an improbable candidate for the detection of ¹³C⁺ fractionation because of the large column density of C⁺ on the line of sight. However, fractionation effects may be observable if the [C II] emission is dominated by the clumpy structure as seen by Hogerheijde et al. (1995) and Lis & Schilke (2003). They found clumps with a density well above 10⁶ cm⁻³ embedded in a more widely distributed “interclump” gas with a density of 10⁴ – 2 × 10⁵ cm⁻³ (Simon et al. 1997). Moreover, the gas in front and behind the main Orion Bar should have a more favorable geometry. By mapping [¹³C II], we were able to distinguish the three regions.

The second PDR is formed by the molecular interface around the ultracompact H II region Mon R2 at a distance of 830 pc (6^h07^m46.2^s, –6°23'08.0"). Due to the larger distance, the PDR is weaker in [C II] than the Orion Bar, in spite of the larger FUV intensity from the central source of about 3 × 10⁵χ₀ (Fuente et al. 2010). The almost spherical PDR geometry around the H II region provides a situation close to the plane-parallel model from Sect. 2.2 when observing the source center, with two PDR layers at high velocities behind and in front of the H II region along one line of sight. The velocity dispersion of up to 10 km s⁻¹ (e.g. Ginard et al. 2012) promises a low optical depth at high integrated line intensities making Mon R2 one of the best candidates to detect an enhanced [C II]/[¹³C II] intensity ratio (Pilleri et al. 2012a). The situation is, however, complicated by the unknown local role of outflows that have been observed on a somewhat larger scale (Xu et al. 2006).

As a third PDR we observed the clump MM2 close to NGC 3603 at a distance of about 6 kpc (Stolte et al. 2006) (11^h15^m10.89^s, –61°16'15.2"), illuminated by a FUV intensity of about 10⁴χ₀ from the OB stars in NGC 3603 (Röllig et al. 2011). The fourth source is the Carina Nebula at a distance of

plied a correction factor to account for the $F = 1 - 1$ transition, which was not covered by the available instrumental bandwidth. With our revised line strengths, the correction factor decreases from 5/4 to 8/7, resulting in a 9.4% increase in the inferred elemental ratio, from the range of 52 – 61 given by Boreiko & Betz (1996) to a range of 57 – 67. This then resolves a small discrepancy, noted by Boreiko & Betz (1996), between the ratio obtained from observations of [¹³C II] and the value of 67 ± 3 inferred from observations of ¹³CO.

about 2.3 kpc (Smith 2006), illuminated by the OB stars in the massive clusters Trumpler 14 and 16 with a FUV flux of about $4 \times 10^3 \chi_0$ (Okada et al. 2012). Here, we observed two interfaces, the Carina North PDR ($10^{\text{h}}43^{\text{m}}35.14^{\text{s}}$, $-59^{\circ}34'04.3''$) close to Trumpler 14, and the Carina South PDR ($10^{\text{h}}45^{\text{m}}11.54^{\text{s}}$, $-59^{\circ}47'34.3''$) south of η Car, including the core IRAS-10430-5931. In NGC3603 and Carina, the PDRs are known to occur at the surface of clumps, partially visible as pillars in the near infrared. Therefore, we expect a behavior matching the clumpy model from Sect. 2.3 that predicted no observable enhancement of the [C II]/[¹³C II] intensity ratio for UV fields above $10^2 \chi_0$.

The last PDR is the northern filament in NGC 7023 ($21^{\text{h}}01^{\text{m}}32.4^{\text{s}}$, $68^{\circ}10'25.0''$) at a distance of 430 pc (van den Ancker et al. 1997) illuminated by the pre-main-sequence B3Ve star HD200775 providing a FUV flux of $1100 \chi_0$ at the position of our observation (Joblin et al. 2010; Pilleri et al. 2012b). Here, previous observations (e.g Gerin et al. 1998) show a smooth density increase towards the filament and a stratified PDR structure so that we may find the situation modelled in Sect. 2.2. The [C II] mapping results have been presented already by Joblin et al. (2010).

All five PDRs were mapped in [C II] using the on-the-fly (OTF) observing mode, however, only the Orion Bar was bright enough to detect [¹³C II] in the map. Therefore, separate deeper dual-beam switch (DBS) measurements were performed towards the given coordinates in the other four PDRs. Unfortunately, the Orion Bar observations used an LO setting that placed the $F = 1 - 1$ transition out of the covered IF range, so that only the $F = 2 - 1$ and $F = 1 - 0$ components were observed there.

The data were calibrated with the standard HIFI pipeline in the Herschel Common Software System (HCSS Ott 2010) in version 9.0 (2226). All data presented here are given on the scale of the antenna temperature corrected for the forward efficiency, T_A^* . The preference for this temperature scale is motivated by the fact that all maps show very extended emission. The T_A^* scale provides correct brightness temperatures if the error beam of the telescope is uniformly filled by emission of the same magnitude as the main beam. The HIFI error beam at 1900 GHz is mainly provided by the side lobes of the illumination pattern appearing at radii of less than two arcminutes (Jellema et al. in prep). Scaling to main-beam temperatures, in contrast, would assume a negligible contribution of the error beam pickup to the measured intensity, increasing the resulting temperatures by a factor 1.39 (Roelfsema et al. 2012). The two scales will bracket the true brightness temperature. As the actual emission decreases with growing distance from the sources, the T_A^* scale will slightly overestimate the error beam contribution and underestimate the brightness temperature, but due to the very extended emission it should be considerably better than the main beam temperature scale. We estimate therefore that the antenna temperature underestimates the brightness temperature by 10-20 %.

The resulting spectra suffer from baseline ripples due to instrumental drifts. They were subtracted using the `HifiFitFringe` task of the HCSS including the baseline option with a minimum period of 200 MHz covering all ripples visible in the spectra. This method attributes structures wider than 200 MHz to instrumental artifacts and all narrower structures to sky signal. In this way we only get reliable intensity information for lines narrower than 30 km s^{-1} , a condition that is met for all our PDRs. In the DBS observations, the resulting spectra also suffered from self-chopping because the chopper throw of 3' often ends at OFF positions that are still contaminated by some emission. This affected the detection of the $F = 2 - 1$ hyperfine component in NGC 3603 and Carina falling into the

range of self-chopping features of the main isotopic line. We tried to circumvent this problem by looking into the individual single-beam switch spectra, that only use one OFF position left or right of the source, not combining them. Although they show different degrees of contamination from the two OFF positions, some contamination always appeared in both spectra, so that we obtained no qualitative improvement with respect to a clear detection of the hyperfine component. Therefore, we show in the following only the dual beam switch spectra providing the better signal-to-noise ratio.

With the high signal to noise ratio of the [C II] line in the Orion Bar map we noticed a small zig-zag structure in reported positions and the resulting Orion Bar map, originating from the alternating direction in the observation of subsequent OTF lines. An ad-hoc correction of the pointing information by $1.4''$, mutually shifting the OTF lines relative to each other, resulted in a straight Orion Bar structure. This correction will be implemented in future versions of the HIFI pipeline, but for this paper the correction just gives an estimate for the pointing accuracy. The original Orion Bar map also suffered from relatively strong emission at the OFF position ($5^{\text{h}}35^{\text{m}}44.92^{\text{s}}$, $-5^{\circ}25'17.1''$) visible as absorption feature in numerous points of the map. A separate observation of the OFF position was performed using the internal HIFI cold load as primary reference and a secondary OFF position more than $12'$ away from the Bar ($5^{\text{h}}35^{\text{m}}55.0^{\text{s}}$, $-5^{\circ}13'18.1''$) as secondary reference. Fortunately, it turned out that the baseline from the subtraction of the cold load spectrum was good enough so that the secondary OFF position did not have to be used because we detected even from this very remote position [C II] emission as bright as 10 K (see Fig. 5) in agreement with the large-scale map of Mookerjea et al. (2003). This has to be considered as a very widely distributed emission floor in the Orion region.

4. Observational results

Table 2 lists the integrated intensities of the [C II] line and the [¹³C II] components for all sources. The relative intensities of the [¹³C II] hyperfine components are roughly consistent with the intensity ratios from Table 1. However, in the observations with the best signal-to-noise ratio, the Orion Bar peak and NGC 7023, we find a somewhat lower $F = 2 - 1 / F = 1 - 0$ ratio of 2 – 2.4 instead of 2.5. The uncertainty of the integrated intensities consist of three contributions: radiometric noise, the definition of the appropriate velocity integration range, and the uncertainty in the baseline subtraction. When measuring the noise in the spectra, we found that its contribution to the total uncertainty is actually negligible compared to the two other sources of uncertainty for all our observations.

The definition of the best integration range asks for a compromise because broad wings in the [C II] profile, in particular in Mon R2, favor very broad integration ranges to trace the whole [C II] emission while the small separation between the [C II] line and the [¹³C II] $F = 2 - 1$ transition and wavy baseline structures ask for narrow integration ranges. As the wings are not detectable in the [¹³C II] components and their intensity ratio forms the main focus of this study, we used common relatively narrow integration ranges here (column 2 of Tab. 2). In this way, we ignore the wing emission that is detectable in the main isotopic line, but compare the same velocity ranges for the isotopic ratios. In the extreme case of Mon R2, the integrated [C II] intensity is higher by 15 K km s^{-1} , i.e. 4 %, compared to the value in Tab. 2 when using a very broad integration range including all the wings and in the Orion Bar the value would be increased by

Table 2. Summary of integrated line intensities from the observations and derived parameters.

source	integration range [km s ⁻¹]	[C II] [K km s ⁻¹]	[¹³ C II] $F = 2 - 1$ [K km s ⁻¹]	$F = 1 - 0$ [K km s ⁻¹]	$F = 1 - 1$ [K km s ⁻¹]	IR^a	$\langle\tau_{[CII]}\rangle$	$N_{C^+}^b$ [10 ¹⁸ cm ⁻²]
Orion Bar, peak	7 – 13	857 ± 5	17.2 ± 1.0	7.8 ± 0.5	–	30 ± 2	1.9 ± 0.2	10.1
Orion Bar, ridge ^c	7 – 13	772 ± 5	12.6 ± 1.0	5.1 ± 0.5	–	38 ± 3	1.3 ± 0.2	7.2
Orion Bar, front ^d	7 – 13	506 ± 7	4.3 ± 0.7	2.1 ± 0.6	–	69 ± 12	0.0 ± 0.4	2.3
Orion Bar, back ^e	7 – 13	529 ± 6	6.3 ± 0.6	2.9 ± 0.6	–	50 ± 6	0.7 ± 0.3	3.9
Mon R2, total	5 – 25	362 ± 5	–	2.9 ± 0.7	0.7 ± 0.5	38 ± 10	1.3 ± 0.6	5.7
Mon R2, blue	5 – 12.5	173 ± 3	–	2.4 ± 0.7	0.8 ± 0.3	20 ± 5	3.2 ± 0.8	4.8
Mon R2, red	12.5 – 25	188 ± 4	–	0.7 ± 0.5	-0.3 ± 0.4	170 ± 120	0.0 ± 0.5	0.9
NGC 3603	10 – 19	130 ± 2	–	1.4 ± 0.2	0.55 ± 0.15	25 ± 5	2.4 ± 0.4	3.6
Carina N	-20 – -5	143 ± 4	–	1.3 ± 0.3	0.7 ± 0.3	27 ± 7	2.2 ± 0.6	5.0
Carina S	-38 – -25	38 ± 2	2.7 ± 0.3 ^f	-0.1 ± 0.3	0.0 ± 0.3	> 22	< 2.9	0.2 ^g
NGC 7023	-1 – 7	91 ± 2	1.07 ± 0.05	0.53 ± 0.07	0.19 ± 0.04	51 ± 6	0.6 ± 0.3	1.0

Notes. ^(a) [C II]/[¹³C II] intensity ratio. From the sum over all [¹³C II] hyperfine components assuming the ratios from Table 1 to correct for non-detected components. ^(b) Assuming a uniform Gaussian velocity profile for C⁺ and ¹³C⁺. ^(c) Average over the ≈ 1000 square-arcsec with $I([C II]) \geq 700$ K km s⁻¹ representing the main Bar emission (see contours in Fig. 4). ^(d) Average over the ≈ 750 square-arcsec with $450 \text{ K km s}^{-1} \leq I([C II]) \leq 650 \text{ K km s}^{-1}$ north-west of the Bar. ^(e) Average over the ≈ 900 square-arcsec with $450 \text{ K km s}^{-1} \leq I([C II]) \leq 650 \text{ K km s}^{-1}$ south-east of the Bar. ^(f) The identification of this emission as [¹³C II] $F = 2 - 1$ is questionable because of the small separation from the [C II] line. It may rather represent a different velocity component. ^(g) Assuming $\tau = 0.0$ to compute the column density.

7 K km s⁻¹, i.e. 1 %, in this way. For the other sources no wing components can be detected due to self-chopping signatures in the spectra (see Fig. 12).

The uncertainty that actually determines the error bars given in Tab. 2 stems from the baseline subtraction in the spectra. Only to a small degree they are given by radiometric noise, but they are dominated by correlated residuals in the baselines that are not easily described by statistic measures. We performed numerical experiments by varying the number of sinusoidal components in the `HifiFitFringe` task between 1 and 4 and changing the size of the window that is masked, i.e. excluded from the baseline fit, from the pure integration range to a range that is about three times wider in five steps. We inspected all baseline fits manually excluding those where self-chopping signatures or line wings affected the fit. The uncertainties in Tab. 2 describe the variation in the remaining sample in terms of the total covered range, i.e. they do not quantify 1σ errors but the extremes of that sample. It is obvious that the relative errors are small for the Orion Bar with narrow lines while they increase with the line width and the resulting larger baseline uncertainty. For the figures shown in the next section we used the subjective “best baseline fit” from the sample.

4.1. Orion Bar

4.1.1. [C II]

[C II] was mapped along a strip perpendicular to the direction of the Bar. Figure 4 shows the overlay of the integrated intensity on the corresponding IRAC 8 μ m image. [C II] shows a very smooth structure without any indication for clumpiness as seen e.g. in the different isotopologues of CO, HCN, HCO⁺, CS and H₂CO by Hogerheijde et al. (1995) and Lis & Schilke (2003) and to a lower degree also in the C91 α carbon radio recombination line by Wyrowski et al. (1997). This indicates that [C II] traces mainly the widely distributed, relatively uniform interclump medium. Position, structure, and overall extent of the [C II] Orion Bar emission are similar to the C91 α radio recombination line map. That map shows, however, a larger contrast and some clumpy substructure within the emission peak. To some degree that may be due to insufficient short-spacing of the in-

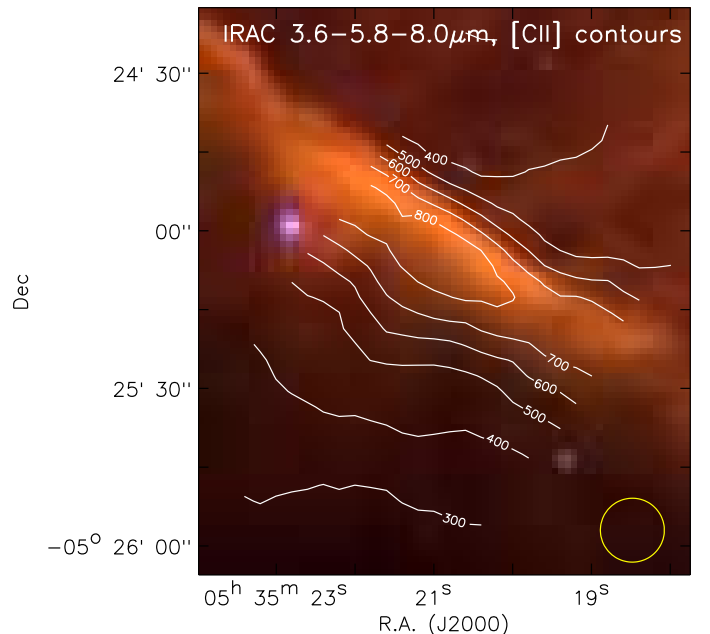


Fig. 4. Integrated [C II] contours over-laid on the false-color IRAC map of the Orion Bar (red: 8.0 μ m: 0–3000 MJy/sr, green: 5.8 μ m: 0–7000 MJy/sr, blue: 3.6 μ m: 0–10000 MJy/sr). [C II] is mapped in a strip perpendicular to the Orion Bar. Intensities are labelled in units of K km s⁻¹. The colors in the IRAC map are provided by the signal in the 3.6, 5.8, and 8 μ m channels. The yellow circle indicates the HIFI beam size.

terferometer data, but it probably also reflects real differences in the excitation of the C⁺. As the C91 α emission depends much more sensitively on the gas density and temperature than [C II] (see e.g. Natta et al. 1994), the ratio of the two lines may provide a way to better characterize the transition between the widely distributed gas and the embedded clumps. The [C II] emission peaks approximately 10'' deeper in the cloud compared to the PAH emission traced by the IRAC 8 μ m map. This coincides approximately with the peak of the H₂ 1-0 S(1) line measured by Walmsley et al. (2000) and correlates very well with the C₂H

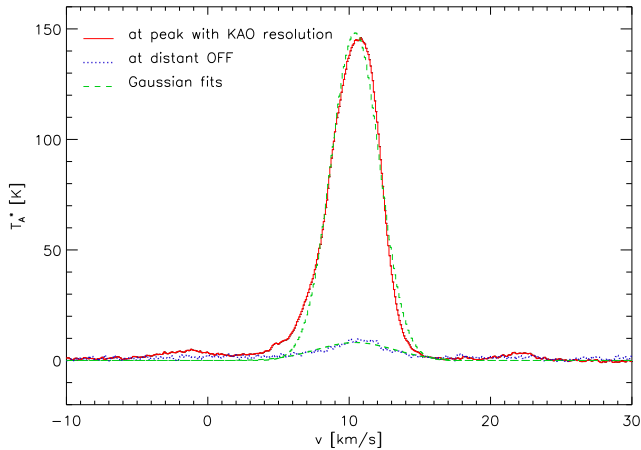


Fig. 5. [C II] profile towards the peak of the Orion Bar emission ($5^{\text{h}}35^{\text{m}}20.6^{\text{s}}$, $-5^{\circ}25'5''$) averaged over a $43''$ (FWHM) Gaussian beam representing the resolution of the previous KAO observations (solid line). The dotted spectrum represents the widely distributed emission as measured on our secondary OFF position $12.3'$ away from the Orion Bar in a region without molecular emission. The dashed lines show Gaussian fits to the two profiles.

emission observed by van der Wiel et al. (2009). The detailed comparison of the stratification in the different lines will be the topic of a forthcoming paper (Makai et al. in prep).

We can compare our data with previous KAO observations of [C II] in Orion. Boreiko et al. (1988) and Boreiko & Betz (1996) obtained frequency-resolved spectra towards $\Theta^1\text{C}$, but not towards the Orion Bar. The spectrally unresolved maps by Stacey et al. (1993) and Herrmann et al. (1997) showed approximately the same integrated intensity at the peak of the Orion Bar and towards $\Theta^1\text{C}$. The $\Theta^1\text{C}$ value from Boreiko & Betz (1996) of $3.8 \times 10^{-3} \text{ erg cm}^{-2} \text{ s}^{-1} \text{ sr}^{-1}$ is, however, 16% lower than the $4.5 \times 10^{-3} \text{ erg cm}^{-2} \text{ s}^{-1} \text{ sr}^{-1}$ derived for the integrated [C II] intensity at the Orion Bar by Herrmann et al. (1997) scaling all intensities to match the previous value from Stacey et al. (1993) towards Orion KL. Figure 5 shows our [C II] HIFI profile towards the peak in the Orion Bar after convolution to the $43''$ resolution of the KAO. The integrated intensity of $585 \text{ K km s}^{-1} = 4.1 \times 10^{-3} \text{ erg cm}^{-2} \text{ s}^{-1} \text{ sr}^{-1}$ falls between the two quoted KAO values. The discrepancy with the lower value from Boreiko & Betz (1996) can be partially explained by self-chopping of the KAO observations in the very extended emission. Our observation of the secondary OFF position (also shown in Fig. 5) gives an estimate for this extended emission providing a 6% correction of the KAO values. The 9% discrepancy with the Herrmann et al. (1997) value could be due to the uncertainty in the error beam pickup discussed above or the scaling method used in their paper.

As we find almost perfect Gaussian profiles for the lines in the Orion Bar (see Fig. 5) we performed Gaussian fits to all [C II] spectra. In Fig. 6 we show the resulting map of amplitudes and widths. As the observations by Boreiko & Betz (1996) indicated partially optically thick lines, we expect that the lines become broader towards the peak of the emission due to optical depth broadening. The map, however, does not show any significant change of the line width across the Orion Bar. The FWHM of the line falls between 4.0 and 4.5 km s^{-1} only turning broader for the more diffuse emission in the north. Consequently, the am-

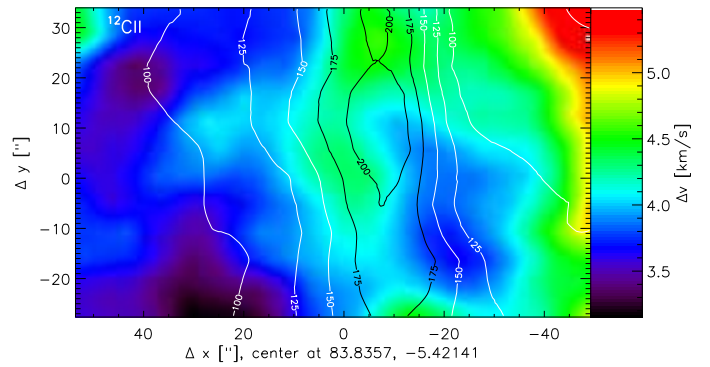


Fig. 6. Contours of the [C II] line peak intensity overlaid on the line width (FWHM) obtained from a Gaussian fit to the [C II] lines at all points in the Orion Bar map.

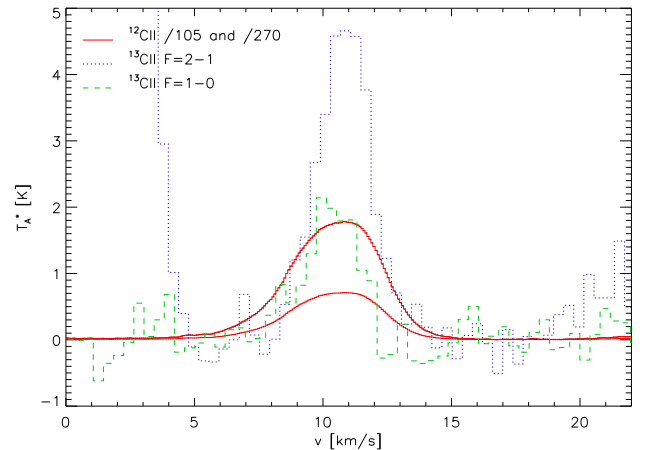


Fig. 7. Average profile of the two strongest [¹³C II] hyper-fine components in the Orion Bar compared to the [C II] profile scaled by factors of $0.625/67$ and $0.25/67$. The profiles were averaged over all pixels with a [C II] integrated intensity above 700 K km s^{-1} .

plitude map gives a perfect match to the integrated line map in Fig. 4. As we confirm the significant optical depth in the following section, this indicates that the [C II] line must be composed of many velocity components which are individually optically thick, instead of a continuous microturbulent medium that only turns optically thick at the largest column density sum. The corresponding map of line velocities only shows a small gradient along the Bar with velocities of about 11 km s^{-1} in the north-east and 10.5 km s^{-1} in the south-west.

4.1.2. [¹³C II]

Due to the narrow line width in the Orion Bar, we are able to detect the $F = 2 - 1$ and $F = 1 - 0$ lines of [¹³C II] without noticeable blending with the [C II] line. Figure 7 shows the line profiles of the two [¹³C II] components when averaged over the region with the brightest emission, i.e. with [C II] intensities of more than 700 K km s^{-1} . For a comparison we have added the corresponding [C II] spectra, scaled by factor of $0.625/67$ and $0.25/67$. This scaling corresponds approximately to the line intensity of the two [¹³C II] transitions that would be expected when we assume the canonical abundance ratio and optically thin lines.

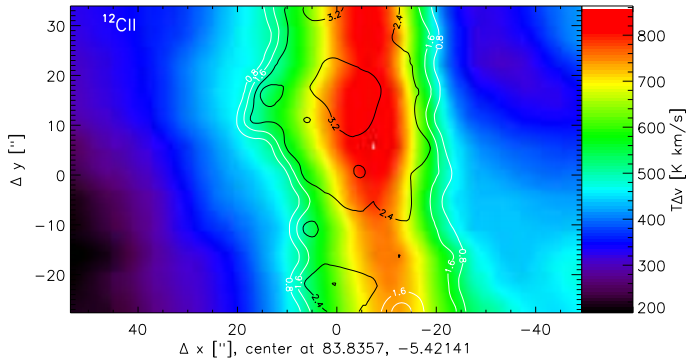


Fig. 8. Contours of the [C II] line center optical depth, derived from the [C II]/[¹³C II] ratio, overlaid on the integrated [C II] intensities observed towards the Orion Bar.

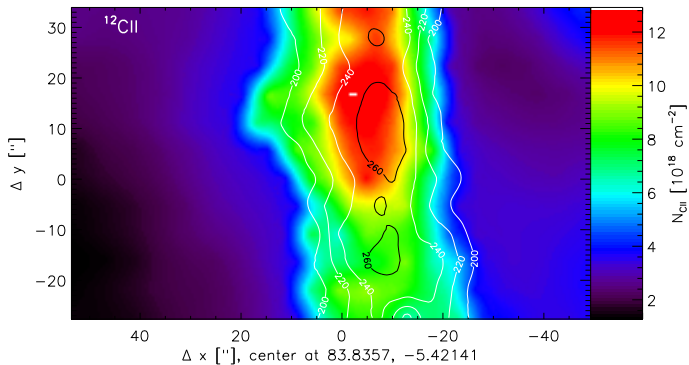


Fig. 9. Contours of the [C II] excitation temperature overlaid on the derived column densities towards the Orion Bar.

When considering the line amplitudes, we find that both hyperfine transitions are approximately 2.5 times brighter than expected from optically thin [C II] emission and the normal isotopic ratio. Assuming the canonical abundance ratio, this corresponds to a line-center optical depth, $\hat{\tau}$ of 2.2. The good signal to noise ratio of the data allows us to perform Gaussian fits to the hyperfine lines over the full map providing a full map of intensity ratios. Using Eq. 5 and assuming no chemical fractionation, we can translate this into a map of optical depths. Figure 8 shows the resulting line center optical depth, $\hat{\tau}$, overlaid on the integrated [C II] intensities. Here, we have added both hyperfine transitions to increase the signal to noise. No reliable values can be derived for $\tau \lesssim 0.8$ as Eq. 5 turns very flat for low optical depths. Hence, all points with lower optical depth have been masked-out. We find a good correlation of the optical depth structure with the intensity map. The map confirms that the area of bright [C II] emission has optical depths above two and the peak optical depth of 3.4 occurs close to the intensity peak, but we also see a small general shift of the optical depth structure relative to the intensity structure away from the exciting Trapezium cluster. This is consistent with the picture of hotter gas at the PDR front and somewhat cooler gas, but a higher column density deeper into the cloud.

To better quantify this, we use Eq. 3 to compute the excitation temperatures, and Eq. 2 together with the optical depth correction in Eq. 5 to compute the total C⁺ column density. The resulting distribution is shown in Fig. 9.⁶ In the range of significant optical depths, the excitation temperatures fall between

⁶ When scaling the measured intensities to the main beam efficiency, i.e. assuming less extended emission, the optical depth does not change,

190 and 265 K. For $\tau \leq 0.8$ we assumed a constant excitation temperature of 190 K and directly used the optically thin approximation of Eq. 2 to compute the C⁺ column density.

Our excitation temperatures are in agreement with the average value of 220 K and 215 K derived by Herrmann et al. (1997) and Sorochenko & Tsivilev (2000), respectively, for the Orion Bar. Interclump gas at this temperature with a density around 10^5 cm^{-3} also explains the C91 α observations by Wyrowski et al. (1997). However, Natta et al. (1994) and Walmsley et al. (2000) obtain much higher temperatures from the radio recombination lines. This could indicate nonthermal emission, dielectronic recombination, or simply different gas components contributing to the [C II] and C91 α emission (Natta et al. 1994; Sorochenko & Tsivilev 2000).

At the scale of the KAO resolution, our approach provides a column density of $7 - 8 \times 10^{18} \text{ cm}^{-2}$ being more than two times higher than the value of Herrmann et al. (1997), consistent with our [C II] optical depth exceeding the value derived by Boreiko & Betz (1996) by about the same factor. The discrepancy can be explained to a large degree by their use of the line-averaged optical depth, underestimating the peak depth by a factor 0.64 for a Gaussian velocity distribution (see Sect. 2.3), and their use of different spectroscopic parameters, as discussed in Sect. 3.1. Our peak C⁺ column density of $13 \times 10^{18} \text{ cm}^{-2}$ implies a configuration where most of the line-of-sight column density of the Orion Bar of $N_{\text{H}} \approx 13 \times 10^{22} \text{ cm}^{-2}$ (e.g. Hogerheijde et al. 1995) forms a PDR with complete ionization of the gas phase carbon – abundance $X(\text{C}) = n(\text{C})/(n(\text{H}) + 2n(\text{H}_2)) = 1.2 \times 10^{-4}$ for dense clouds (Wakelam & Herbst 2008). A surprising result is, however, the relatively large C⁺ column density in front and behind the Bar. Molecular line observations (e.g. Hogerheijde et al. 1995; van der Werf et al. 1996) deduced column densities that are a factor ten lower than in the Bar. Consequently, at least half of the [C II] emission in the veil must stem from atomic, more diffuse material.

Fig. 9 also shows the relative shift between the column density and the excitation temperature distributions by 5–8'' with the higher temperatures towards the illuminating source. The new observations thus resolve a temperature gradient in C⁺ consistent with the overall stratified structure of the Orion Bar PDR. The resulting intensity profile then represents a convolution of density and temperature structures.

4.1.3. Line averages

To verify the dependence of the results on the assumption of the Gaussian velocity distribution, we repeated the analysis for selected subregions when considering the line-averaged [C II]/[¹³C II] intensity ratio, i.e. $\langle \tau \rangle$ instead of $\hat{\tau}$. This is also the only possible analysis for the other sources where the signal-to-noise ratio is lower and the line profiles are highly structured so that the assumption of a Gaussian velocity distribution is clearly violated. The use of the line averaged optical depths, $\langle \tau \rangle$, corresponds to the assumption of a macro-turbulent situation, where [C II] turns independently optically thick in all velocity channels, while the $\hat{\tau}$ method assumes a microturbulent Gaussian velocity distribution for all tracers, where [C II] turns optically thick only in the line center. A preference for one of the methods is only possible based on detailed knowledge of the source structure. The $\langle \tau \rangle$ results for all sources are included in the last two columns in Table 2.

but the excitation temperature and C⁺ column densities increase by 30% relative to the values given here.

For the Orion Bar, the $\langle\tau\rangle$ results always fall below the column densities from the line-center optical depth by 30–35 % in spite of the almost Gaussian line profiles. A possible cause is the systematic difference in the line width between the $^{13}\text{C II}$ and the [C II] lines going beyond the expected optical-depth broadening. As seen in the average spectrum shown in Fig. 7, but also in the map of $^{13}\text{C II}$ line widths corresponding to Fig. 6, the $^{13}\text{C II}$ line is always 1.0–1.5 km s^{-1} narrower than the [C II] line. As a consequence, the intensity ratio is even larger than the standard elemental isotopic ratio in the line wings (well visible in the blue wing in Fig. 7). Together with the constant [C II] line width discussed in the previous section, the enhanced intensity ratio in the wings indicates different velocity distributions for C^+ and $^{13}\text{C}^+$ so that neither the $\hat{\tau}$ method nor the $\langle\tau\rangle$ method can provide accurate results. The 30–35 % of the emission remaining in the wings of the [C II] line when fitting it with the profile of the $^{13}\text{C II}$ lines provide an estimate for the accuracy of the method.

The $\langle\tau\rangle$ values from the average spectra in Table 2 also confirm the spatial gradient of the column densities discussed for Fig. 9. When analyzing the bright gas in front and behind the Orion Bar by selecting all pixels with a [C II] intensity between 450 and 650 K km s^{-1} north-west, i.e. in the direction of the illuminating Trapezium stars, and south-east of the Bar, we find significantly higher optical depths behind the Bar while the gas in front of the Bar is typically hotter by about 20 K, but thinner by a factor 1.7.

None of the average spectra show an indication for an enhanced C^+/C^+ fractionation ratio. This also applies to the spectra from the veil in front and behind the Bar where we were not able to detect a significant deviation from the elemental abundance ratio due to the relatively larger baseline uncertainties at lower intensities of the $^{13}\text{C II}$ lines. Our $^{13}\text{C II}$ observations are consistent with negligible carbon fractionation and an enhanced optical depth of the main isotopic line for high column densities. This is in agreement with a previous detection of the $^{13}\text{C I}$ $F = 5/2 - 3/2$ transition by Keene et al. (1998) in a selected clump where the observed $^{13}\text{C}/\text{C}$ ratio showed no fractionation effect in contrast to the complementary observations for $^{13}\text{C}^{18}\text{O}$ and C^{18}O .

An indication for an enhanced fractionation ratio is, however, seen in the velocity structure when considering the wings of the bright line profiles. The broader [C II] lines showing enhanced [C II]/ $^{13}\text{C II}$ intensity ratio in the wings (e.g. in Fig. 7) indicate that an additional gas component, with broader velocity dispersion and enhanced fractionation ratio, thus invisible in $^{13}\text{C II}$, contributes to the [C II] profiles. The constancy of the [C II] line width then could be explained by the mutual compensation of the relatively larger contribution from the low-velocity dispersion Orion Bar material with the optical depth broadening there. To sustain the enhanced intensity ratio, the broad velocity gas component should have moderate gas densities of $10^3 - 10^4 \text{ cm}^{-3}$ and face moderate UV fields ($\chi \approx 10^3$, see Sect. 2).

4.2. Mon R2

4.2.1. [C II]

The [C II] OTF map of Mon R2 consists of a single strip across the ultracompact H II region from north-east to south-west (see Fuente et al. 2010). In Fig. 10 we show the position-velocity diagram for that cut. This is important for understanding the origin of the components of the spectral profile in the comparison with the $^{13}\text{C II}$ lines. We find a ring-like structure in position-

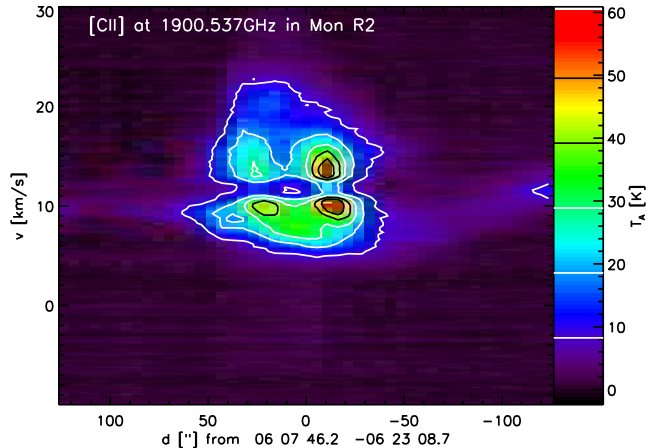


Fig. 10. Position-velocity diagram of the [C II] line for the measured cut through the Mon R2 PDR.

velocity space, with two well separated components towards the center of the H II region. A better understanding of the position velocity structure can be obtained by combining this information with equivalent maps in several other tracers (Pilleri et al. 2012a). In particular the comparison with water lines, that show up in absorption in the blue component but in emission in the red component, suggests that the diagram traces a PDR around the H II region that is accelerated by the radiative pressure from the central source, so that the back side is red-shifted and the front blue shifted relative to the systemic velocity of the medium. However, the observations show the existence of some asymmetry between the expanding and receding layer and part of the central dip could also stem from self-absorption in the optically thick line.

4.2.2. $^{13}\text{C II}$

The dual-beam-switch observations of the $^{13}\text{C II}$ lines were performed at the center position of the OTF strip (position 0 in Fig. 10), i.e. not at the peak of the [C II] emission. Future follow-up observations at the peak position will provide a better accuracy.

Figure 11 shows the line profiles of the $^{13}\text{C II}$ components compared to the corresponding [C II] spectrum, scaled by the factor 0.25/67 and 0.125/67 indicating the expected strength of the $F = 1 - 0$ and $F = 1 - 1$ hyperfine components in case of optically thin emission and a canonical abundance ratio (see Sect. 3.1). Due to the large width of the [C II] line, the $F = 2 - 1$ component falls in the wing of the [C II] emission, so that we cannot estimate its strength. The striking result for the other two transitions is the large difference in the spectral shape compared to the main isotopic line. The two hyperfine components are consistent with each other in terms of the spectral shape, peaking at about 9 km s^{-1} and in terms of the intensity ratio of about a factor two. The peak agrees with a flat-top emission part of the [C II] line that would be characteristic for optically thick emission and is about three times brighter than the scaled blue [C II] component. This is not reflected in the average optical depth $\langle\tau\rangle$ derived from the integrated line in Table 2 due to the strong mutual difference in the line shapes. To get an estimate for the two main velocity components, we have split the integration interval at 12.5 km s^{-1} and include the corresponding results in Table 2. This increases the relative uncertainties, but allows to derive in-

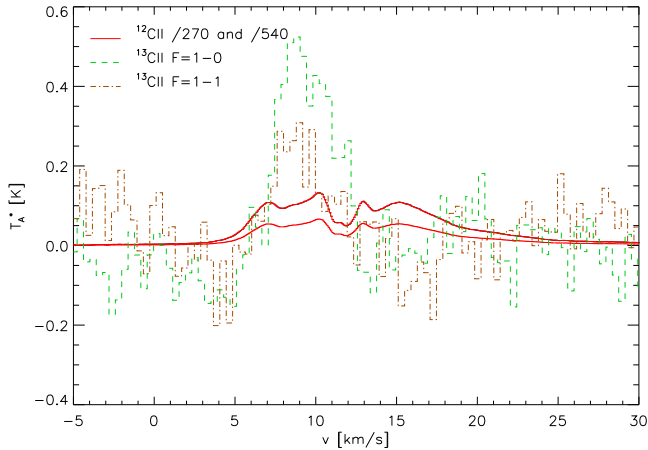


Fig. 11. Comparison of the profiles of the [¹³C II] hyperfine lines in Mon R2 with the [C II] profile in the same spectrum scaled by the factors 0.25/67 and 0.125/67. The [¹³C II] F=2-1 component is blended with the main isotopic line so that is not shown here.

dependent quantitative results for the components that show a very different behavior. For the blue-shifted foreground component, we find the highest [C II] optical depth in our sample.

The big surprise is the complete absence of redshifted emission from the back of the H II region in [¹³C II]. The red-shifted [C II] line has approximately the same brightness as the blue component, but any possible [¹³C II] emission must be weaker than expected from optically thin emission and normal abundance ratios. For both hyperfine components an emission at the 0.1 K level can be excluded in spite of the baseline uncertainties. This indicates the direct observation of fractionation in a PDR driving an enhanced ¹²C⁺/¹³C⁺ ratio. However, when considering the extreme uncertainties in Table 2, stemming from all possible baseline subtractions and the possibility that the redshifted [C II] line might be optically thin while the blueshifted line has an optical depth > 3, the error bars for the ¹²C⁺/¹³C⁺ fractionation ratio still cover the standard elemental isotopic ratio so that even this case is not unambiguous.

4.3. NGC 3603, Carina, and NGC 7023

Figure 12 shows the spectra for NGC 3603, Carina North, and NGC 7023, obtained in the same way as Fig. 11 for Mon R2. As discussed in Sect. 3.2, in NGC 3603 and Carina the $F = 2 - 1$ component falls into a [C II] spectral feature resulting from self-chopping in the observation, so that it cannot be resolved. The two weaker components are resolved. There is no indication for a spectral difference with respect to the [C II] line and the mutual line ratio reflects the expected value from Sect. 3.1. In both sources, the [¹³C II] lines are about 2.5 times stronger than expected from optically thin [C II] emission and the normal abundance ratio. The increase indicates an optical depth in the main isotopic line of 2.2 – 2.4.

The equivalent observation of the Carina South PDR, provided no detections of [¹³C II]. At the frequency of the $F = 2 - 1$ transition we find a weak emission component, but we rather attribute this to a separate [C II] velocity component in the complex velocity profile. As the [C II] line brightness was more than three times weaker than in the other sources, the non-detection is consistent with the expected line strength in the optically thin

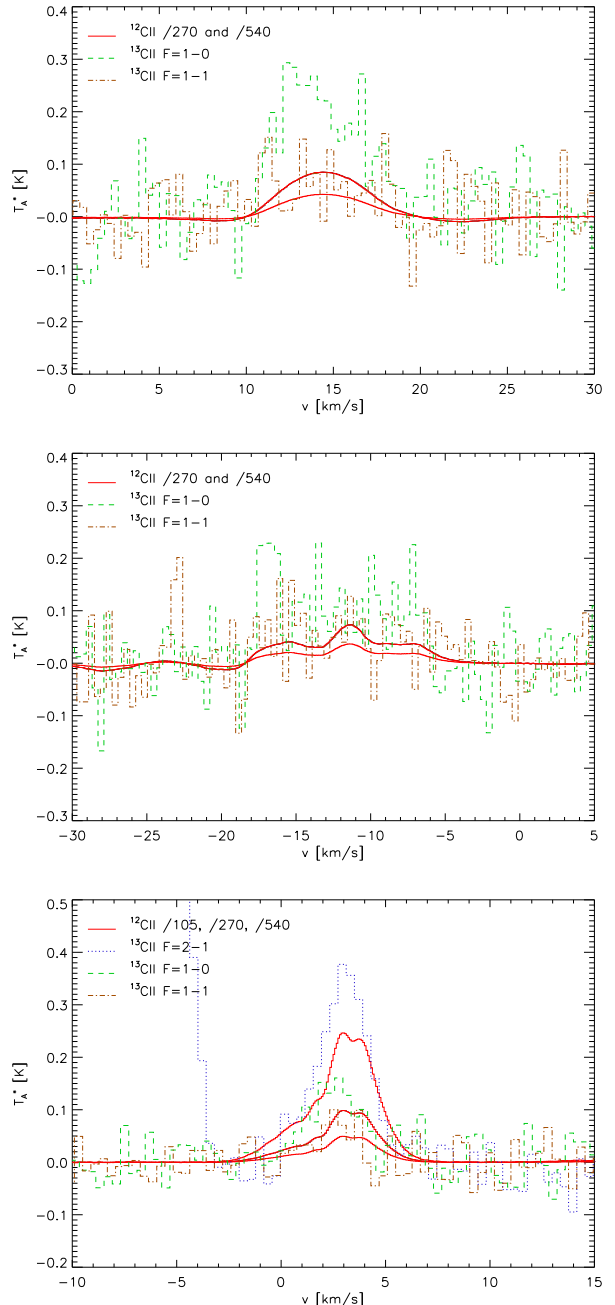


Fig. 12. Comparison of the profiles of the [¹³C II] hyperfine lines in NGC 3603 MM2 (upper panel), the Carina North PDR (central panel), and NGC 7023 North (lower panel) with the [C II] profiles from the same positions scaled by the factors corresponding to optically thin emission and the standard abundance ratio for the resolved hyperfine components. For NGC 3603 MM2 and Carina North, the [¹³C II] F=2-1 component falls into a self-chopping feature of the main isotopic line so that is not shown here.

case or cases with a moderate [¹³C II] line enhancement as in the other sources.

The narrow [C II] line in NGC 7023 is well separated from the [¹³C II] $F = 2 - 1$ component, so that this is the only observation in which we resolve all three hyperfine components. Moreover the narrow lines provide a very small uncertainty for the line intensity from the baseline subtraction so that we get

quite accurate relative intensities. The average optical depth enhancement of the $^{13}\text{C II}$ lines is moderate, but we also find a significantly different behavior of different velocity components resolved in the [C II] line. The $^{13}\text{C II}$ lines mainly trace the component at 2.8 km s^{-1} corresponding to the molecular material in the PDR (see e.g. Gerin et al. 1998). Here, we find a significant optical depth of the [C II] line in terms of a decreased $[\text{C II}]/[^{13}\text{C II}]$ intensity ratio. The component at 4 km s^{-1} was identified as separate filament by Fuente et al. (1996) and associated with ionized material in the cavity by Joblin et al. (2010). It is also seen in $^{13}\text{C II}$ and shows an intensity ratio corresponding to the elemental isotopic ratio. Finally there is a high velocity wing with velocities around 0 km s^{-1} . This component may show an increased $^{12}\text{C}^+ / ^{13}\text{C}^+$ fractionation ratio through $^{13}\text{C II}$ intensities below the scaled [C II] intensity for all three hyperfine components. However, our signal-to-noise ratio is not good enough to derive a definite statement on the $[\text{C II}]/[^{13}\text{C II}]$ intensity ratio in that wing. Due to the almost Gaussian velocity components, the estimate of the C^+ column density from the integrated line parameters should be a reasonable average by slightly underestimating the optical depth from the PDR and slightly overestimating the contribution from the ionized gas in the cavity. For a total column density $N_{\text{H}} \approx 1.3 \times 10^{22} \text{ cm}^{-2}$ at the position of our observation (Joblin et al. 2010) this indicates that more than half of the carbon in the gas phase is in the form of C^+ .

5. Discussion

The detection of carbon fractionation under dense cloud conditions remains difficult. For the two species involved in the most important carbon fractionation reaction, C^+ and CO, the lines of the main isotopologue are often optically thick with a considerable uncertainty in the optical depth. Consequently, it is hard to determine the absolute column density and the $\text{CO}/^{13}\text{CO}$ or $\text{C}^+ / ^{13}\text{C}^+$ ratio. Our observations and simulations have confirmed this general knowledge for the $\text{C}^+ / ^{13}\text{C}^+$ ratio. Observations of $^{13}\text{C}^{18}\text{O}$ are a possible way out, but challenging due to the low line intensities, biased towards high column densities, and they cannot trace the impact of isotope-selective photodissociation provided by the self-shielding of the main isotopologue.

Our model predictions for PDRs indicate that the observed fractionation ratio in all tracers is dominated by the chemical fractionation reaction (C 1) while isotopic-selective photodissociation plays a minor role. The chemical fractionation increases the $\text{C}^+ / ^{13}\text{C}^+$ ratio relative to the elemental isotopic ratio in the gas. In terms of the observable $[\text{C II}]/[^{13}\text{C II}]$ ratio, this could lead to an increase by a factor of a few under favorable conditions. They can be provided by inner layers of moderate density, moderate UV PDRs or by dense gas that is exposed to low UV fields like clumps in an inhomogeneous PDR, embedded in and partially shielded by a thinner interclump medium. The main condition for an observable increase of the $[\text{C II}]/[^{13}\text{C II}]$ ratio is, however, that geometry and velocity distribution prevent a large [C II] optical depth. In most geometries, the conditions providing an increased isotopic ratio are paired with high optical depths of the [C II] line that rather reduces the $[\text{C II}]/[^{13}\text{C II}]$ intensity ratio below the canonical value.

Our observations show that most of the [C II] emission must stem from a widely distributed, low-density component in PDRs, being more smoothly distributed than many high-density tracers. Only in Mon R2, where the H II region is still expanding into the surrounding high-density core, a probably relatively homo-

geneous high-density PDR is formed. The observational results on the $[\text{C II}]/[^{13}\text{C II}]$ intensity ratio roughly follow the predictions from the models in Sect.2 without providing enough statistics for a qualitative confirmation yet. For most of the PDRs, the average $[\text{C II}]/[^{13}\text{C II}]$ intensity ratio is reduced compared to the isotopic ratio due to the optical thickness of the [C II] line. Details strongly depend on the exact geometry. Assuming the standard elemental ratio for the $\text{C}^+ / ^{13}\text{C}^+$ abundance ratio, we can measure the optical depth and consequently the C^+ column density through the intensity ratio. The optical depth of the main isotopic line varies considerably across the line profile and between the different PDRs, showing peak values above three for the Orion Bar and Mon R2.

Indications for an increased $[\text{C II}]/[^{13}\text{C II}]$ intensity ratio are found when studying details of the line profiles allowing to distinguish different velocity components in the same source. In three cases, we find components showing C^+ fractionation in a PDR. Unfortunately, none of them allows to unambiguously quantify the degree of fractionation due to the large error bars from the noise and baseline uncertainties (see Table 2). The clearest case is the non-detection of $^{13}\text{C II}$ in the red-shifted component in Mon R2. If we interpret the red component as the receding inner backside of the expanding H II region, it represents a dense, face-on PDR layer which should be at least partially optically thick in [C II]. As the front side shows the same integrated [C II] intensity, but no fractionation and a very high [C II] optical depth instead, the actual configuration must be asymmetric. The situation is even more puzzling as our models predict negligible fractionation for this high-UV field PDR. Further high-resolution observations are required to understand why the red-shifted material differs from the front material. The second case is provided by the wings of the line profiles in the Orion Bar, probably created by diffuse gas with a broader velocity distribution. It may represent extended, possibly diffuse H II gas in the Orion veil. To confirm this origin, deeper integrations in positions apart from the Orion Bar are needed. A final case may be given by the blue wing material seen in NGC 7023. However, in all three cases the step from a pure detection of fractionation to a full quantitative assessment requires observations with a somewhat better signal-to-noise ratio than obtained here.

Acknowledgements. This work was supported by the *Deutsche Forschungsgemeinschaft*, DFG project number Os 177/1–1 and SFB 956 C1. Additional support for this paper was provided by NASA through an award issued by JPL/Caltech and by Spanish program CONSOLIDER INGENIO 2010, under grant CSD2009-00038 Molecular Astrophysics: The Herschel and ALMA Era (ASTROMOL). We thank Paul Goldsmith and an anonymous referee for many helpful comments.

HIFI has been designed and built by a consortium of institutes and university departments from across Europe, Canada and the US under the leadership of SRON Netherlands Institute for Space Research, Groningen, The Netherlands with major contributions from Germany, France and the US. Consortium members are: Canada: CSA, U.Waterloo; France: CESR, LAB, LERMA, IRAM; Germany: KOSMA, MPfR, MPS; Ireland, NUI Maynooth; Italy: ASI, IFSI-INAF, Arcetri-INAF; Netherlands: SRON, TUD; Poland: CAMK, CBK; Spain: Observatorio Astronómico Nacional (IGN), Centro de Astrobiología (CSIC-INTA); Sweden: Chalmers University of Technology - MC2, RSS & GARD, Onsala Space Observatory, Swedish National Space Board, Stockholm University - Stockholm Observatory; Switzerland: ETH Zürich, FHNW; USA: Caltech, JPL, NHSC.

References

- Bergin, E. A. & Herschel Hexos Team. 2011, in IAU Symposium, Vol. 280, IAU Symposium, 93P
- Boreiko, R. T. & Betz, A. L. 1996, ApJ, 467, L113+
- Boreiko, R. T., Betz, A. L., & Zmuidzinas, J. 1988, ApJ, 325, L47
- Burgh, E. B., France, K., & McCandliss, S. R. 2007, ApJ, 658, 446

- Cooksey, A. L., Blake, G. A., & Saykally, R. J. 1986, *ApJ*, 305, L89
- de Graauw, T., Helmich, F. P., Phillips, T. G., et al. 2010, *A&A*, 518, L6+
- Draine, B. T. 1978, *ApJS*, 36, 595
- Flannery, B. P., Roberge, W., & Rybicki, G. B. 1980, *ApJ*, 236, 598
- Flower, D. R. & Launay, J. M. 1977, *Journal of Physics B Atomic Molecular Physics*, 10, 3673
- Fuente, A., Berné, O., Cernicharo, J., et al. 2010, *A&A*, 521, L23+
- Fuente, A., Martin-Pintado, J., Neri, R., Rogers, C., & Moriarty-Schieven, G. 1996, *A&A*, 310, 286
- Garstang, R. H. 1995, *ApJ*, 447, 962
- Gerin, M., Phillips, T. G., Keene, J., Betz, A. L., & Boreiko, R. T. 1998, *ApJ*, 500, 329
- Ginard, D., González-García, M., Fuente, A., et al. 2012, *A&A*, 543, A27
- Graf, U. U., Simon, R., Stutzki, J., et al. 2012, *A&A*, in press
- Herrmann, F., Madden, S. C., Nikola, T., et al. 1997, *ApJ*, 481, 343
- Hogerheijde, M. R., Jansen, D. J., & van Dishoeck, E. F. 1995, *A&A*, 294, 792
- Joblin, C., Pilleri, P., Montillaud, J., et al. 2010, *A&A*, 521, L25
- Keene, J., Schilke, P., Kooi, J., et al. 1998, *ApJ*, 494, L107+
- Langer, W. D., Graedel, T. E., Frerking, M. A., & Armentrout, P. B. 1984, *ApJ*, 277, 581
- Langer, W. D. & Penzias, A. A. 1990, *ApJ*, 357, 477
- Langer, W. D. & Penzias, A. A. 1993, *ApJ*, 408, 539
- Launay, J.-M. & Roueff, E. 1977, *Journal of Physics B Atomic Molecular Physics*, 10, 879
- Lis, D. C. & Schilke, P. 2003, *ApJ*, 597, L145
- Liszt, H. S. 2007, *A&A*, 476, 291
- Menten, K. M., Reid, M. J., Forbrich, J., & Brunthaler, A. 2007, *A&A*, 474, 515
- Mookerjee, B., Ghosh, S. K., Kaneda, H., et al. 2003, *A&A*, 404, 569
- Natta, A., Walmsley, C. M., & Tielens, A. G. G. M. 1994, *ApJ*, 428, 209
- Okada, Y., Pilleri, P., Berné, O., et al. 2012, *A&A*, submitted, .
- Ossenkopf, V., Röllig, M., Kramer, C., et al. 2011, in *EAS Publications Series*, Vol. 52, *EAS Publications Series*, ed. M. Röllig, R. Simon, V. Ossenkopf, & J. Stutzki, 181–186
- Ott, S. 2010, in *Astronomical Society of the Pacific Conference Series*, Vol. 434, *Astronomical Data Analysis Software and Systems XIX*, ed. Y. Mizumoto, K.-I. Morita, & M. Ohishi, 139–+
- Phillips, T. G., Huggins, P. J., Wannier, P. G., & Scoville, N. Z. 1979, *ApJ*, 231, 720
- Pilbratt, G. L., Riedinger, J. R., Passvogel, T., et al. 2010, *A&A*, 518, L1+
- Pilleri, P., Fuente, A., Cernicharo, J., et al. 2012a, *A&A*, 544, A110
- Pilleri, P., Montillaud, J., Berné, O., & Joblin, C. 2012b, *A&A*, 542, A69
- Roelfsema, P. R., Helmich, F. P., Teyssier, D., et al. 2012, *A&A*, 537, A17
- Röllig, M., Abel, N. P., Bell, T., et al. 2007, *A&A*, 467, 187
- Röllig, M., Kramer, C., Rajbahak, C., et al. 2011, *A&A*, 525, A8+
- Röllig, M. & Ossenkopf, V. 2012, *A&A*, submitted, paper I, .
- Sakai, N., Saruwatari, O., Sakai, T., Takano, S., & Yamamoto, S. 2010, *A&A*, 512, A31
- Schaefer, H. F. & Klemm, R. A. 1970, *Phys. Rev. A*, 1, 1063
- Sheffer, Y., Rogers, M., Federman, S. R., Lambert, D. L., & Gredel, R. 2007, *ApJ*, 667, 1002
- Simon, R., Stutzki, J., Sternberg, A., & Winnewisser, G. 1997, *A&A*, 327, L9
- Smith, N. 2006, *MNRAS*, 367, 763
- Sonnentrucker, P., Welty, D. E., Thorburn, J. A., & York, D. G. 2007, *ApJS*, 168, 58
- Sorochenko, R. L. & Tsivilev, A. P. 2000, *Astronomy Reports*, 44, 426
- Stacey, G. J., Jaffe, D. T., Geis, N., et al. 1993, *ApJ*, 404, 219
- Stolte, A., Brandner, W., Brandl, B., & Zinnecker, H. 2006, *AJ*, 132, 253
- Stutzki, J., Bensch, F., Heithausen, A., Ossenkopf, V., & Zielinsky, M. 1998, *A&A*, 336, 697
- van den Ancker, M. E., The, P. S., Tjin A Djie, H. R. E., et al. 1997, *A&A*, 324, L33
- van der Werf, P. P., Stutzki, J., Sternberg, A., & Krabbe, A. 1996, *A&A*, 313, 633
- van der Wiel, M. H. D., van der Tak, F. F. S., Ossenkopf, V., et al. 2009, *A&A*, 498, 161
- Visser, R., van Dishoeck, E. F., & Black, J. H. 2009, *A&A*, 503, 323
- Wakelam, V. & Herbst, E. 2008, *ApJ*, 680, 371
- Walmsley, C. M., Natta, A., Oliva, E., & Testi, L. 2000, *A&A*, 364, 301
- Wiese, W. & Fuhr, J. 2007, *J. Phys. Chem. Ref. Data*, 36, 1287
- Wilson, N. J. & Bell, K. L. 2002, *MNRAS*, 337, 1027
- Wilson, T. L. 1999, *Reports on Progress in Physics*, 62, 143
- Wyrowski, F., Schilke, P., Hofner, P., & Walmsley, C. M. 1997, *ApJ*, 487, L171
- Xu, Y., Shen, Z.-Q., Yang, J., et al. 2006, *AJ*, 132, 20